CORNELL UNIVERSITY

Center for Radiophysics and Space Research

ITHACA, N. Y.

[redacted]

CRSR 611

A NUMERICAL CIRCULATION MODEL WITH TOPOGRAPHY FOR THE MARTIAN SOUTHERN HEMISPHERE

Clifford Mass and Carl Sagan

[redacted]

OCTOBER 1975

A NUMERICAL CIRCULATION MODEL WITH TOPOGRAPHY FOR THE MARTIAN SOUTHERN HEMISPHERE

Clifford Mass* and Carl Sagan

Laboratory for Planetary Studies

Cornell University

Ithaca, New York 14853

* Present address: Department of Atmospheric Sciences,
University of Washington
Seattle, Washington 98105

ABSTRACT

A quasi-geostrophic numerical model, including friction, radiation, and the observed planetary topography, is applied to the general circulation of the Martian atmosphere in the southern hemisphere at latitudes south of about 35°. Near equilibrium weather systems developed after about 5 model days. To avoid violating the quasi-geostrophic approximation, only 0.8 of the already smoothed relief was employed. Weather systems and velocity fields are strikingly tied to topography. A 2mb middle latitude jet stream is found of remarkably terrestrial aspect. Highest surface velocities, both horizontal and vertical, are predicted in western Hellas Planitia and eastern Argyre Planitia, which are observed to be preferred sites of origin of major Martian dust storms. Mean horizontal velocities > 30 m s^{-1} and vertical velocities > 0.2 m s^{-1} are found just above the surface velocity boundary layer. When consideration is taken of scaling to full topography and the probable gustiness of Martian winds, it seems very likely that the general circulation is adequate, at certain times and places, to transport dust from the surface of Mars, as observed. Certain sources and sinks of vertical dust streaming are suggested; the entire south circumpolar zone appears to be a dust sink in winter.

1. Introduction

Leovy and Mintz (1969) constructed the first numerical model of atmospheric circulation on Mars. They employed a primitive equation two-level model with radiative-convective heating and cooling. Allowance was made for the condensation of carbon dioxide on the surface and the consequent release of latent heat. At winter solstice, maximum meridional winds of about 8 m/s for both atmospheric levels were found; at equinox, the corresponding values were about 2 m/s. On the other hand, the maximum zonal winds at high altitude at solstice reached about 70 m/s at 45° North latitude, while at equinox the maximum zonal winds were about 25 m/s. The corresponding maximum "surface" winds -- corresponding to the region just above the surface boundary layer -- were estimated to be about 20 m/s at solstice and about 10 m/s at equinox. No topography was included.

However, the Martian surface is know to exhibit major elevation differences (Sagan et al., 1967; Sagan and Pollack, 1968; Pettengill et al., 1973; Downs et al., 1973; Conrath et al., 1973; Kliore et al., 1973; Hord et al., 1974). Over continental dimensions, elevation differences comparable to a scale height occur on Mars; and over scales of a few hundred kms elevation differences of 2 or 3 scale heights exist. Under these conditions, winds produced by relief seem able in restricted locales on Mars to increase the mean winds by factors of two to three over the mean wind velocities expected in the absence of relief (Gierasch and Sagan, 1971).

Wind velocities at half surface pressure level in excess of 80 m/s were therefore predicted at certain seasons and locales, and a range of observational consequences of such high winds predicted (Sagan et al., 1971). Time-variable streaks and splotches on the Martian surface have been interpreted in terms of windblown dust produced by such high winds (Sagan, et al., 1972; 1973; 1974; Veverka et al., 1974).

The work reported in the present paper is a simple numerical experiment on the general circulation of the Martian atmosphere with topography included. The analysis is restricted to the Southern hemisphere only. The assumed topography is shown in Figure 1, and is based upon Mariner 9 UVS, IRIS and S-Band occultation experiments. Near the South Pole the assumed elevations reflect some Mariner 9 television stereoscopic results as well (Blasius, 1974). Since some inconsistencies in the results of the various Mariner 9 and groundbased radar topographies still exist, the Southern hemisphere Martian topography adopted in these calculations may not correspond precisely to the true circumstances. Nevertheless, the general relief seems to be sufficiently well-established that the influence of topography on atmospheric circulation can be tested.

2. Structure and Equations

The physics of this two-level model is based upon the assumption of a hydrostatic, adiabatic, quasi-geostrophic, ideal gas atmosphere entirely composed of carbon dioxide. Radiative transfer between the atmosphere, space and ground is included in the model, as is surface friction. No provision is made for the latent heat of phase change of atmospheric constitutents or for albedo differences over the Martian surface.

The model's vertical structure, shown in Table 1, is one in which the geopotential heights of two pressure surfaces, at 2 and 4 mb, are predicted, while at the 3mb level the vertical velocity w_{3mb} is diagnosed. At the 6mb surface an orographic vertical velocity w_{6mb} is computed using the surface topographic gradient and the 4mb surface horizontal velocity. Finally, at the upper surface the vertical velocity is assumed to be zero. The set of four predictive and diagnostic equations used in this model can be derived using the hydrostatic, adiabatic, quasi-geostrophic and ideal gas approximations (see, e.g., Haltiner, 1971; Thompson, 1961).

First, at the upper, 2mb, surface the partial differential equation for predicting changes in the geopotential heights of that surface is

$$\nabla^2\left(\frac{\partial z}{\partial t}\right)_{2mb} + \frac{1}{2} J(z_{2mb}, \phi_{2mb} + f) - \frac{f^2 d^2}{gm\Delta p} (w_{3mb}) = 0 \qquad (1)$$

where J is the Jacobean operator; f is the Coriolis parameter $= 2\Omega\sin\theta$; θ is the latitude; d is the distance between grid points; m is the map scale factor which corrects the distances for the projection used (in this case polar stereographic) to the real world values; ϕ_{2mb} is the geostrophic relative vorticity on the 2mb surface $= (g/f)\ \nabla^2 z_{2mb}$; Δp is the difference in pressure between the two geopotential surfaces (2mb); and w_{3mb} is the vertical velocity of the 3mb surface in units of pressure/time.

On the lower 4mb surface the equation for geopotential change is similar but has additional terms including friction and the surface orographic vertical velocity, w_{6mb}:

$$\nabla^2\left(\frac{\partial z}{\partial t}\right)_{4mb} + \frac{1}{2} J(z_{4mb}, \phi_{4mb} + f)$$

$$- \frac{f^2 d^2}{gm\Delta p} (w_{6mb} - w_{3mb}) + \left(\frac{\partial Fy}{\partial x} - \frac{\partial Fx}{\partial y}\right) = 0. \qquad (2)$$

Here g is the gravitational acceleration $= 372$ cm s^{-2} and F_y and F_x are the y and x frictional components at the surface. They are treated in a manner similar to that employed by Leovy and Mintz (1969), i.e.,

$$\vec{F} = \frac{2g}{(p_s - p_t)} \vec{\tau}_s \qquad (3)$$

where $(p_s - p_t)$ is the difference in pressure between the upper and lower levels. The surface stress is written

$$\tau_s = \rho_s U^{*2} (V_s / |V_s|) \tag{4}$$

where the friction velocity U^* is

$$U^* = C_m |V_s| \tag{5}$$

V_s is the horizontal wind at the surface (6mb), which is derived from a linear extrapolation of the winds at the 2 and 4mb levels, and C_m^2 is the momentum drag coefficient. Assuming a stable stratification, it has the value 0.9×10^{-3} (cf. Leovy and Mintz, 1969). ρ_s is the atmospheric density at the surface. This lower boundary friction is the principal means of dissipation of thermal energy.

The vertical velocity of the 3mb surface is diagnosed and the radiative effects are introduced into the model by means of the omega equation:

$$\begin{aligned} &\sigma \nabla^2 w_{3mb} + \frac{f^2 d^2}{gm^2 (\Delta p)^2} (w_{6mb} - 2w_{3mb}) \\ &= \frac{g}{8fd^2 \Delta p} \nabla^2_m J(z_{4mb} + z_{2mb}, z_{4mb} - z_{2mb}) \\ &- \frac{1}{4\Delta p} [J(z_{4mb}, \phi_{4mb} + f) - J(z_{2mb}, \phi_{2mb} + f)] \\ &- \nabla^2 \frac{RQ}{gpc_p} = 0. \end{aligned} \tag{6}$$

σ is the static stability = $(g\rho\theta)^{-1}(\partial\theta/\partial p)$; θ is the potential temperature = $T(p_o/p)^{\kappa}$, where $\kappa = C_p/R$; p_o/p = (6mb/3mb) = 2; R is the gas constant and C_p is the specific heat of CO_2 at constant pressure. A value of -4.14324×10^{-3} m^7 erg^{-2} was employed for σ, 0.188 $\times 10^7$ ergs gm^{-1} for R and 0.874 $\times 10^7$ ergs gm^{-1} $(°K)^{-1}$ for C_p.

Q, the heating or cooling rate is written as a simplified version of the radiative term found in Blumsack, Gierasch and Wessel's (1973) model of the Martian atmospheric structure:

$$Q = q_{solar} + q_{planetary} \tag{7}$$

The solar heating is found from the relation

$$q_s = 0.216 \times 10^6 \ (45\xi^{\frac{1}{4}} + 65.3\xi) \ °K \ cm^{-2} sec^{-1},$$

where arccos ξ is the solar zenith angle.

The planetary term q_p is

$$q_p = \left(\frac{g}{C_p}\right)\left[\frac{C}{p\,(1-s^2)^{\frac{1}{2}} + D}\right]\left[\frac{s}{(1-s^2)^{\frac{1}{2}}}\right]\pi\,[B_{\frac{1}{4}} - B(1^-)]$$

$$-\left(\frac{g}{C_p}\right)\left[\frac{C}{ps + D}\right]\pi\,B(0^+) \tag{8}$$

Here, $s = \frac{1}{4}$; the two radiation parameters are $C = 55$ cm^{-1} and $D = 383$ dyne cm^{-2}; and B is the Planck function at the center of the 15μ band, i.e.,

$$B = \frac{3495}{\exp(960/T)-1} \text{ [erg cm}^{-1}\text{sec}^{-1}\text{]} \tag{9}$$

B_*, $B(0^+)$ and $B(1^-)$ denote the Planck function of the ground and the top and base of the atmosphere, respectively. Thus, the first term of eq. (8) describes the heating or cooling by the ground and the second term describes heat loss into space.

At the lower boundary the orographic vertical velocity is computed from

$$w_{6mb} = - \rho_s g(V_{4mb} \nabla h) \tag{10}$$

∇h is the gradient of the topography and V_{4mb} is the horizontal velocity on the 4mb surface.

Finally, in order to diagnose the mid-atmospheric temperature throughout the simulation the thickness equation was used, i.e.,

$$\bar{T} = \frac{\Delta z \; g}{R \ln 2} \tag{11}$$

where $\bar{T}$ is the average temperature between the 2mb and 4mb surfaces and Δz is the altitude difference between the two surfaces.

3. Numerical Methods

The simulations were made on a 33 x 27 grid covering the majority of the non-equatorial area of the southern hemisphere of Mars. The grid spacing was 202.85 km and the projection used was a polar stereographic, true at 60°S. The omega equation and the two geopotential predictive equations were solved by a Liebmann overrelaxation method in which the computer continuously guesses at a solution, tests if the error is below a certain tolerance, and, if it is not, subtracts or adds by an amount slightly greater than the actual error (cf. Haltiner, 1971; Thompson, 1961).

For stability a time step of 30 minutes and an Arakawa Jacobean was used. Dealing with the boundaries proved more difficult but excellent results were realized by using cyclic boundaries in which surface features could pass off one edge to reappear on another. This was effected by first splitting both the outside rows of the active simulation area and those rows adjacent and exterior to them (see Figure 2). Then the following procedure was adopted for each of the four sides: each outside half row (not in the active simulation area) takes on the values of the diagonally opposite half row located in the active simulation row adjacent to it. Thus in Figure 2 point A takes on the parameter value of B, point C takes on the value at D, point E takes on the value of F, point M takes on the value at N, and so on through that side and the other three sides. To avoid boundary errors, all results

are restricted to latitudes poleward of 30°S, and the outermost latitude circle shown on our polar sterographic projection is 40°S.

The solar zenith angles at the various grid points were allowed to vary diurnally so as to more closely simulate the true heating. Furthermore, these angles could also be varied to simulate the seasons. All simulations begin with an isothermal atmosphere (winter, 185°K; spring, 190°K; summer, 200°K), and with a latitudinally prescribed ground temperature.

The simulations were generally performed for 7.5 or 8.5 days, the limiting factor being computing costs rather than model stability. On the Cornell IBM 360/65 an 8.5 day simulation took approximately 40 minutes of central processing time.

4. Validity of the Results

Since the frictional and radiative time constants of the Martian atmosphere are short, ≈ 2-3 days, it is expected that a simulation of 7.5 or 8.5 days should give definitive results. It was in fact observed that in all simulations a near-equilibrium situation did establish itself within 4.5 days into the simulation (see Figure 3).

Another question deals with the validity of the non-geostrophic terms for heating, friction and, most significant, orographic vertical velocity. The first two terms are not of large magnitude and should pose no problems. However, the effect of the large vertical orographic velocities on the validity of the model must be examined. We define a nondimensional vertical velocity $w^* \equiv w/W$, where W is the vertical velocity scale = $f_o U^2/g$. Here f_o is the mean Coriolis parameter over the latitudes in question and U is the mean horizontal velocity scale. When

$$w^* << Ro \equiv U/f_o L \qquad (12)$$

where L is a characteristic distance scale, the quasi-geostrophic approximation remains valid. More specifically, it can be shown (Phillips, 1963) for orographic vertical velocities, that an additional condition for the validity of the approximation is the following relation connecting the Rossby number, Ro, the atmospheric scale height, H, and the height, h_{max}, of the largest

topographic feature:

$$h_{max} < (Ro)\ H \qquad (13)$$

We adopt H ≈ 8 km. For Mars Ro ≈ 0.25 - 0.50, although for large slopes (∿ 1 percent) the Rossby number approaches unity (cf. Gierasch and Sagan, 1973). These conditions are satisfied if we can assure smaller slopes with heights ranging less than one-half a scale height. Since the actual Martian topography is so rough that these conditions are not fulfilled, numerical methods of smoothing and scaling were employed. For most of the runs a linear relief scaling of 0.8 was used with a nine point smoother. This proved quite effective. As a test, however, we made a few runs without smoothing or scaling and found the model to be dramatically less stable; clearly the quasigeostrophic approximation was failing under conditions of realistic Martian relief.

Because the quasigeostrophic approximation fails at equatorial latitudes, the calculation of heating rate does not include the solar radiation intercepted by the Martian surface at low southern latitudes. To perform a correction, we assume that there is negligible interhemispheric heat transfer and that there are no systematic dependences of albedo on latitude. (The latter assumption is in fact strongly contradicted by the data, and the region between 35°S and the equator has a marked concentration of low albedo regions). A straightforward

geometric calculation shows that the ratio of the insolation between 0 and 35°S to that between 35 and 90°S at winter noon is about 2.4. The meridional heat flux is, to first order, proportional to the product of the meridional wind and the equator-to-pole temperature gradient, and therefore to the square of the meridional wind. Thus, if the wind is proportional to the square root of the heat flux, our horizontal and vertical winds should both be corrected by a factor of $2.4^{\frac{1}{2}} \approx 1.5$. Because of the topography truncation and the albedo assumption, the mean winds derived are probably lower limits on their actual values.

5. Results

The principal topographic features of Figure 1 are the prominent basin in Hellas Planitia (near 290°W, 59°S), a shallower elongated depression centered in Argyre Planitia (near 40°W, 45°S), and a depression offset from the pole (near 110°W, 75°S). Hellas and Argyre are frequently reported to be connected with Martian dust storms, and one objective of this study was to examine topography-connected weather systems and velocity fields in these locales. Because of the possibility that there is a permanent dust pall in these basins (Sagan et al., 1971) they may be substantially deeper than the depths adopted from IRIS and UVS Mariner 9 data in Figure 1, in which case the weather systems and velocity fields generated by these basins should be yet more pronounced. Figure 1 also displays extended plateaux on the Noachis/Mare Serpentis boundary (near 345°W, 35°S) and in a broad region centered on Thaumasia Fossae, south of Solis Lacus (near 90°W, 40°S). While future refinements of the Martian topography may alter some of the details of our results, the general character of the results should remain valid.

In Figure 4 are exhibited numerical results on the development of Martian weather systems in winter at the 4mb level. Geopotential heights are given for seven steps in the development of the system, from 0.5 days to 7.5 days, at which time the

convergence of the calculations is evident. Weather systems whose positions appear to be connected to topography in Figure 4g include the high near Noachis, and the extension of the 3.6 km geopotential surface into Hellas. The weather system is also characterized by a stable polar low. The corresponding 7.5 day result for summer is shown in Figure 5a, where the high and both lows appear to have no direct connection with the topography. The corresponding 8.5 day result for spring equinox is displayed in Figure 5b. Here there is a pronounced low in Western Hellas; a high in Eastern Argyre; a high on the Noachis/Mare Serpentis plateau; and a low in the polar depression.

In general, at the 4mb surface a regime of closed-off regions of low and high geopotential develop. Many of these weather systems, especially in the winter and spring simulations, are approximately stationary. That their positions were determined by topography was conclusively established by varying the relief. A marked strengthening of stationary system was observed as the topography scaling factor was increased. These results should be compared with the topography-independent weather maps of Leovy and Mintz (1969, Figures 19a and b).

The 2mb weather maps of our calculations are shown for winter and summer solstices and for spring equinox in Figure 6. The corresponding horizontal velocities for the winter solstice map are exhibited in Figure 7. An upper level jet stream with maximum velocities of 45 m s^{-1} is evident. Its location at

middle latitudes and the order of magnitude of its velocities are both strikingly similar to the terrestrial case. Also analogous to the Earth's jet stream is the greater intensity of the winds during winter, with wind maxima found in closed-off jet cores.

Horizontal velocities at the 4mb level are shown in Figure 8 at Spring Equinox for the cases of no topography and 0.8 the full topography of Figure 1. It is apparent that inclusion of topography greatly complicates the velocity field as well as increasing the number of regions experiencing the highest velocities. This trend continues for surface velocities. In Figure 9 we see the Winter Solstice velocity field for 0.8 full topography. The highest velocities shown are about 30 m s^{-1}, and correlate very well with the locales of highest velocity for the 4mb surface (Figure 8b), in the spring. This correlation is another demonstration of the high degree of topographic control of Martian winds. Since we know that there are locales many km higher and lower than the smoothed topography of Figure 1, occasional velocities two or three times larger than those exhibited in Figure 9 may be implied. Of the five locales in Figure 9 of highest velocity, all but one are in the western interior slopes of Hellas Planitia, encompassing the Hellesponti Montes; in the center of Noachis; and in the southeastern quadrant of Argyre Planitia. (The fifth is on the border of Eridania and Mare Tyrrhenum.) But these are just the regions in which large dust storms have been

observed over the course of a century of groundbased observations of the planet. While the calculations of Figure 9 are for Winter Solstice the strong degree of topographic control of the highest winds suggests that these will be the locales of highest winds for all seasons. Recent calculations of the horizontal winds above the velocity bou layer necessary to lift dust from the Martian surface range from about 25 to about 80 m s^{-1} (Sagan and Veverka, 1976; see also Sagan et al., 1973). The results of the calculations of the present paper appear to be in the required range, even without invoking the tail of the velocity time distribution function (gusts). To the extent that the higher velocities mentioned are required for dust mobility, topographic generation of the highest winds is even more strongly indicated.

Huss (1974) has summarized a range of available information on terrestrial wind velocity distribution functions. Because of the steeper temperature gradients on Mars, terrestrial gustiness should provide a lower limit on Martian gustiness. The results imply that for a 15 m/s mean horizontal velocity on Mars there will be a 10^{-3} probability of a gust, for a minute's duration and a mile of surface, of velocity 40 m/s. Extrapolation suggests that where the mean wind is 30 m/s there is a 10^{-3} probability of such a gust of velocity 70 m/s. Thus, a reasonable allowance for our topography truncation, forced on the calculations by the quasigeostrophic approximation, and likely levels of Martian gustiness, imply that Martian general circulation topographic winds are entirely adequate to produce saltation and suspension

of aerosols on Mars.

The vertical velocities at the surface for winter, spring and summer are shown in Figure 10. The vertical velocities for the same three seasons at the 3mb level are shown in Figure 11. The highest upward velocities in spring and summer are found in western Hellas/Hellesponti Montes, which is also a region of high upward velocity in winter. The highest winter velocities are found in northeastern Argyre. These highest upward velocities are about 0.1 to 0.2 m s^{-1}. From a universal scaling between drag coefficient and Reynolds number, Sagan and Bagnold (1975) have calculated the modified Stokes fall velocities under a range of Martian conditions. The vertical velocities derived in the present paper then correspond to suspension of particles 10 to 20 μm in diameter. Such particles, falling out from an

altitude of 10 km, will reach the ground in about a day. Thus, their continued presence requires continued lifting by the winds. On the other hand, particles about 1μm in diameter have a characteristic fallout time from 10 km altitude of about 10^7s, which is the typical duration of a major Martian dust storm, such as the one experienced by Mariner 9. Likewise 1μm is the typical grain diameter deduced for the 1971 dust storm from a range of different techniques (see, e.g., Hartmann and Price, 1974). Thus it appears that the vertical and horizontal wind components in Western Hellas and Eastern Argyre produce copious amounts of suspendible dust each year. The large particles fall out rapidly, not far from their sites or origin, but the smaller particles are carried over much of the planet before they sediment out. In general the vertical velocities on Mars appear often to be high enough to cause suspension of μm diameter particles; the reason that the planet is not perpetually dust-covered is that the horizontal winds are only infrequently high enough to produce saltation and suspension. These calculations suggest that major and minor dust storms both should be a common occurrence on Mars, a conclusion in apparent accord with recent observational experience.

Locales of preferred downward velocity are also of some interest. For example, in all seasons eastern Argyre appears to be a source of suspendible dust, and western Argyre a sink. There may of course be interior circulation of dust within the Argyre basin (Sagan et al., 1971). The polar depression appears to be a source of suspendible dust in spring, and a sink in

summer and winter. The entire south circumpolar zone appears to be a dust sink in winter (Figure 10a), a fact which may be related to the probably depositional polar laminae (Murray et al., 1973).

Acknowledgment

We are grateful to P. Gierasch, K. Blasius and S. Blumsack for helpful discussions. This research was supported in part by the Planetology Program Office of NASA, under Grant 33-010-220.

TABLE 1
Structure of the Model

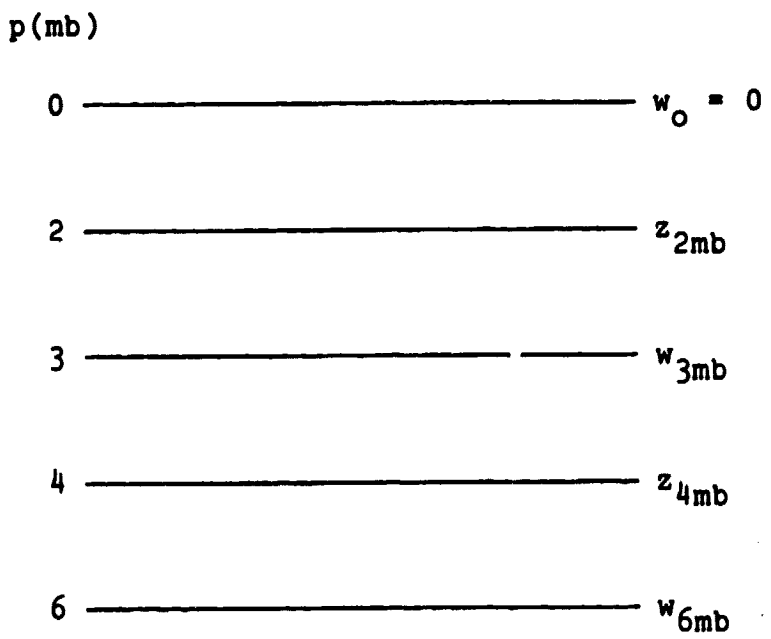

References

Blasius, K. (1974): Private communication.

Blumsack, S. L., P. J. Gierasch and W. R. Wessel, (1973): An analytical and numerical study of the Martian planetary boundary layer over slopes. J. Atmos. Sci., 30, 66-82.

Conrath, B., R. Curran, R. Hanel, V. Kunde, W. Maguire, J. Pearl, J. Pirraglia and J. Welker (1973): Atmospheric and surface properties of Mars obtained by infrared spectroscopy on Mariner 9. J. Geophys. Res. 78, 4267-4278.

Downs, G. S., R. M. Goldstein, R. R. Green, G. A. Morris, and P. E. Reichley (1973): Martian topography and surface properties as seen by radar: The 1971 opposition. Icarus 18, 8-21.

Gierasch, P. J. and C. Sagan (1971): A preliminary assessment of Martian wind regimes. Icarus 14, 312-318.

Haltiner, G. J. (1971): Numerical Weather Prediction, Wiley, New York.

Hartmann, W. K. and M. J. Price (1974): Mars: Clearing of the 1971 dust storm. Icarus 21, 28-34.

Hord, C. W., K. E. Simmons and L. K. McLaughlin (1974): Mariner 9 ultraviolet spectrometer experiment: Pressure-altitude measurements on Mars. Icarus 21, 292-302.

Huss, P. O. (1974): Estimation of distributions and maximum values of horizontal winds speeds. J. Appl. Met. 13, 647-653.

Kliore, A. J., G. Fjeldbo, B. L. Seidel, M. J. Sylas and P. M. Woiceshyn (1973): S-band radio occultation measurements of the atmosphere and topography of Mars with Mariner 9: Extended mission coverage of polar and intermediate latitudes. J. Geophys. Res. 78, 4331-4351.

Leovy, C. and Y. Mintz (1969): Numerical simulation of the atmospheric circulation and climate of Mars. J. Atmos. Scis. 26, 1167-1190.

Murray, B. C., L. Soderblom, J. Cutts, R. Sharp, D. Milton and R. Leighton (1972): Geological framework of the south polar region of Mars. Icarus 17, 328-345.

Pettengill, G. H., I. I. Shapiro and A. E. E. Rogers (1973): Topography and radar scattering properties of Mars. Icarus 18, 22-28.

Phillips, Norman. A. (1963): Geostrophic motion. Reviews of Geophysics, 1, 123-176.

Sagan, C.,J. B. Pollack and R. M. Goldstein (1967): Radar doppler spectroscopy of Mars: I. Elevation differences. Astron. J. 72, 20-34.

Sagan, C. and J. B. Pollack (1968): Elevation differences on Mars. J. Geophys. Res. 73, 1372-1387.

Sagan, C., J. Veverka and P. J. Gierasch (1971): Observational consequences of Martian wind regimes. Icarus 15, 253-278.

Sagan, C. J. Veverka, P. Fox, R. Dubisch, J. Lederberg, E. Levinthal, L. Quam, R. Tucker, J. B. Pollack and B. A. Smith (1972): Variable Features on Mars: Preliminary Mariner 9 Television Results. Icarus 17, 346-372.

Sagan, C., J. Veverka, P. Fox, R. Dubisch, R. French, P. J. Gierasch, L. Quam, J. Lederberg, E. Levinthal, R. Tucker, B. Eross and J. B. Pollack (1973): Variable Features on Mars II: Mariner 9 Global Results. J. Geophys. Res. 78, 4163-4196.

Sagan, C., J. Veverka, R. Steinbacher, L. Quam, R. Tucker and B. Eross (1974): Variable Features on Mars. IV. Pavonis Mons. Icarus 22, 24-47.

Sagan, C. and R. A. Bagnold (1975): Fluid transport on Earth and aeolian transport on Mars. Icarus, in press.

Sagan, C. and J. Veverka (1976): Albedo variations on Mars. In preparation.

Thompson, P. O. (1961): Numerical Weather Analysis and Prediction, Macmillan, New York.

Veverka, J., C. Sagan, L. Quam, R. Tucker, and B. Eross (1974): Variable features on Mars III: Comparison of Mariner 1969 and Mariner 1971 photography. Icarus 21, 317-368.

Figure Captions

Figure 1: Polar stereographic projection of adopted Martian southern hemisphere topography. The outermost circumpolar circle corresponds to latitude 40°S; the circles here and in subsequent such diagrams are spaced in 10° latitude intervals. The topography exhibited here, compiled from a variety of Mariner 9 data, is smoothed, and considerably greater elevation differences actually exist.

Figure 2: Parameterization scheme for cyclic boundaries in the active simulation area. See text for details.

Figure 3: Stability of numerical solutions after several model days for three different Martian seasons.

Figure 4: Winter solstice weather systems at the 4mb level. The contours are geopotential heights in kms. Development of systems is shown for elapsed times between 0.5 days (4a) and 7.5 days (4g). Highs and lows are indicated.

Figure 5: Weather systems at the 4mb level for summer solstice after 7.5 days (5a) and for spring equinox after 8.5 days (5b).

Figure 6: Weather systems at the 2mb level for winter solstice after 7.5 days (6a), for spring equinox after 8.5 days (6b), and for summer solstice after 7.5 days (6c).

Figure 7: Horizontal velocity field in m/s at 2mb level for winter solstice after 7.5 days.

Figure 8: Horizontal velocity field in m/s at 4mb level for spring equinox after 7.5 days. Calculations are shown for no topography (8a) and for 80% of the full (smoothed) topography adopted in Figure 1 (8b).

Figure 9: Horizontal velocity field in m/s just above velocity boundary layer for the Martian surface. Calculations are for winter solstice after 7.5 days and assume 80% of the full topography.

Figure 10: Vertical velocity field in cm/s just above velocity boundary layer for the Martian surface. Calculations are after 5.5 days for winter solstice (10a), spring equinox (10b), and summer solstice (10c). Solid contours indicate upward flow, dashed contours downward flow.

Figure 11: Vertical velocity field in cm/s at the 3mb surface after 5.5 days for winter solstice (11a), spring equinox (11b), and summer solstice (11c). Solid contours indicate upward flow, dashed contours downward flow.

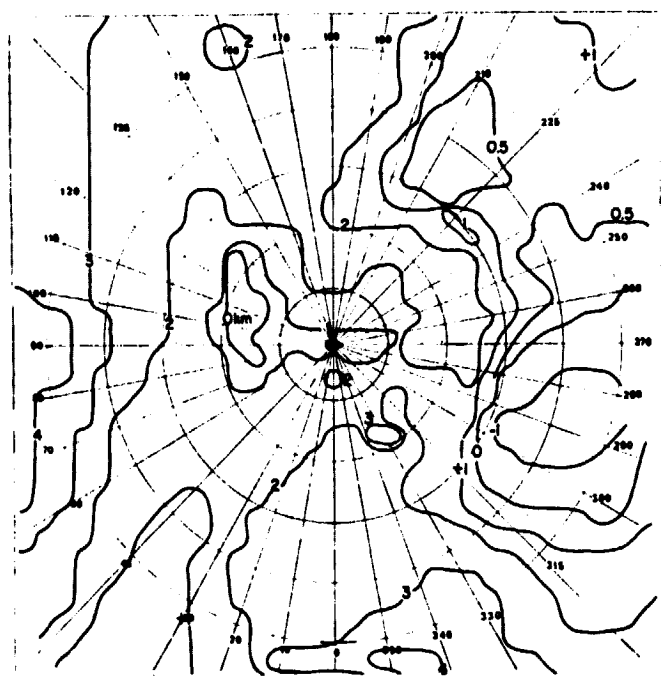

Figure 1

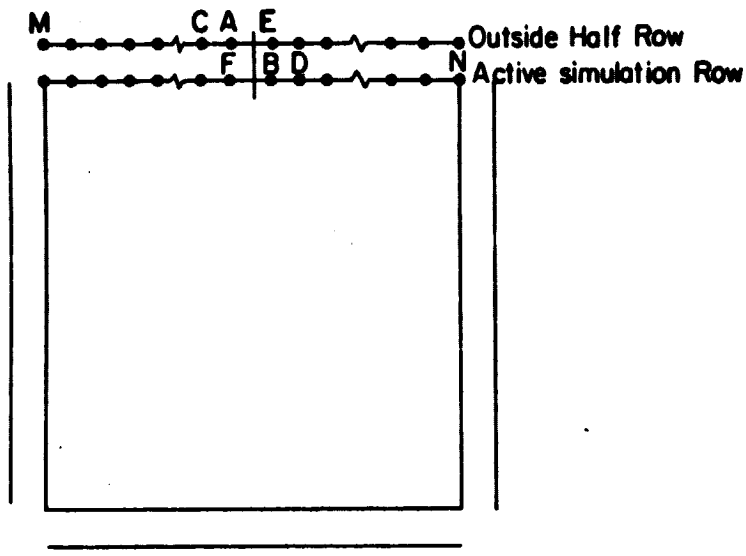

Figure 2

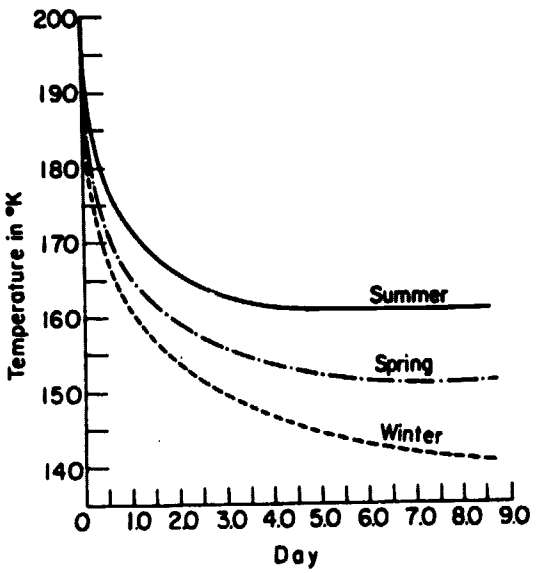
200
190
180
170
160
150
140
Temperature in °K
Summer
Spring
Winter
0
1.0
2.0
3.0
4.0
5.0
6.0
7.0
8.0
9.0
Day

Figure 3

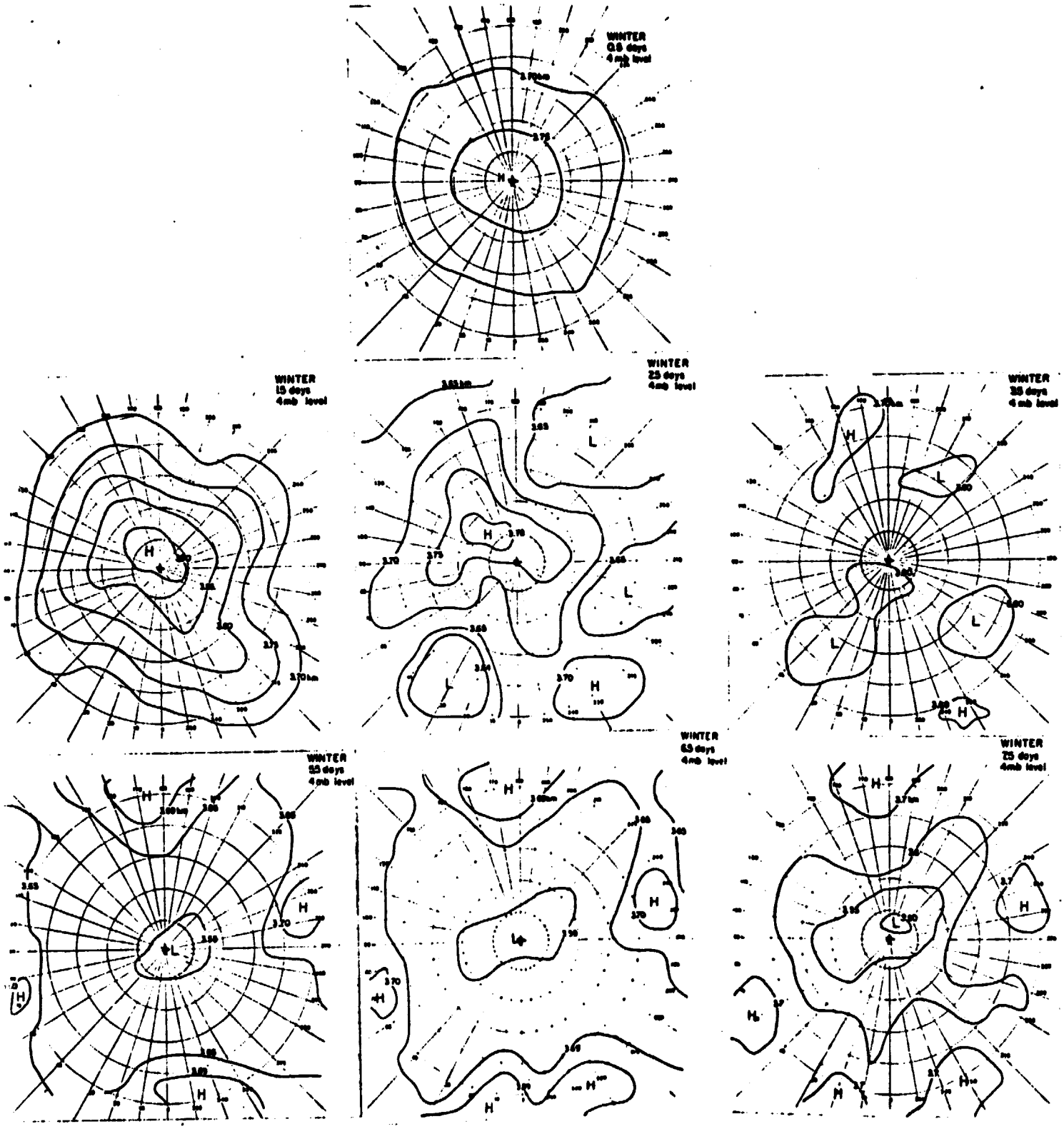

Figure 4

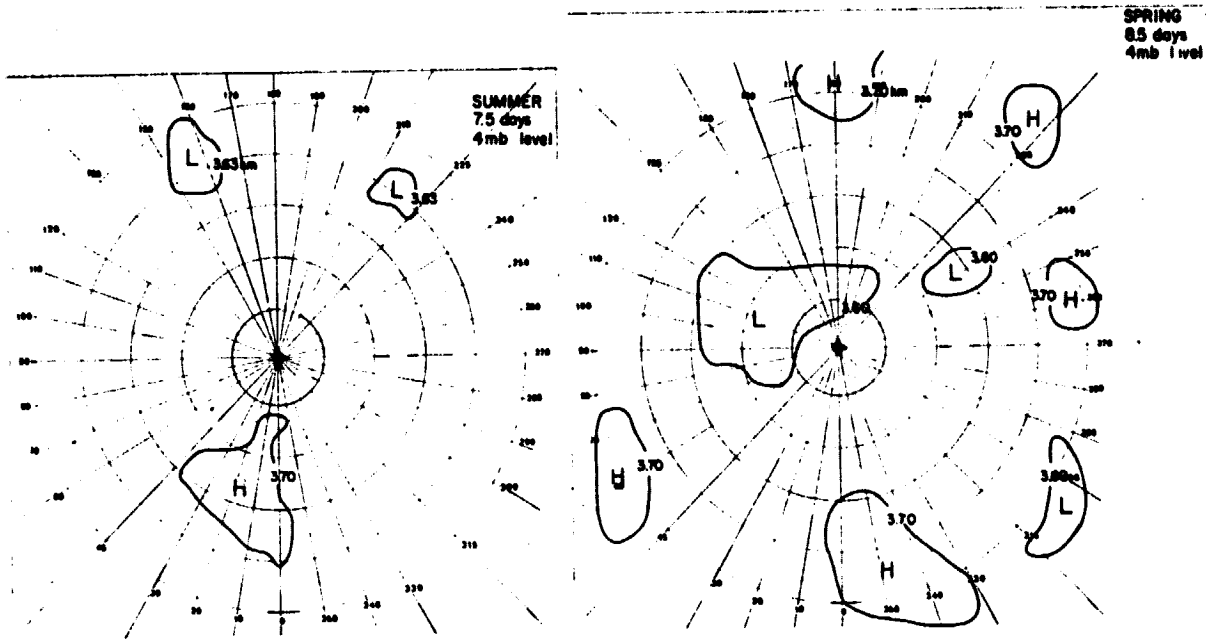
SUMMER
7.5 days
4mb level
L
3.63km
L
3.63
H
3.70
SPRING
8.5 days
4mb level
H
3.70
L
3.60
H
3.70
L
3.60
H
3.70
H
3.70
L

Figure 5

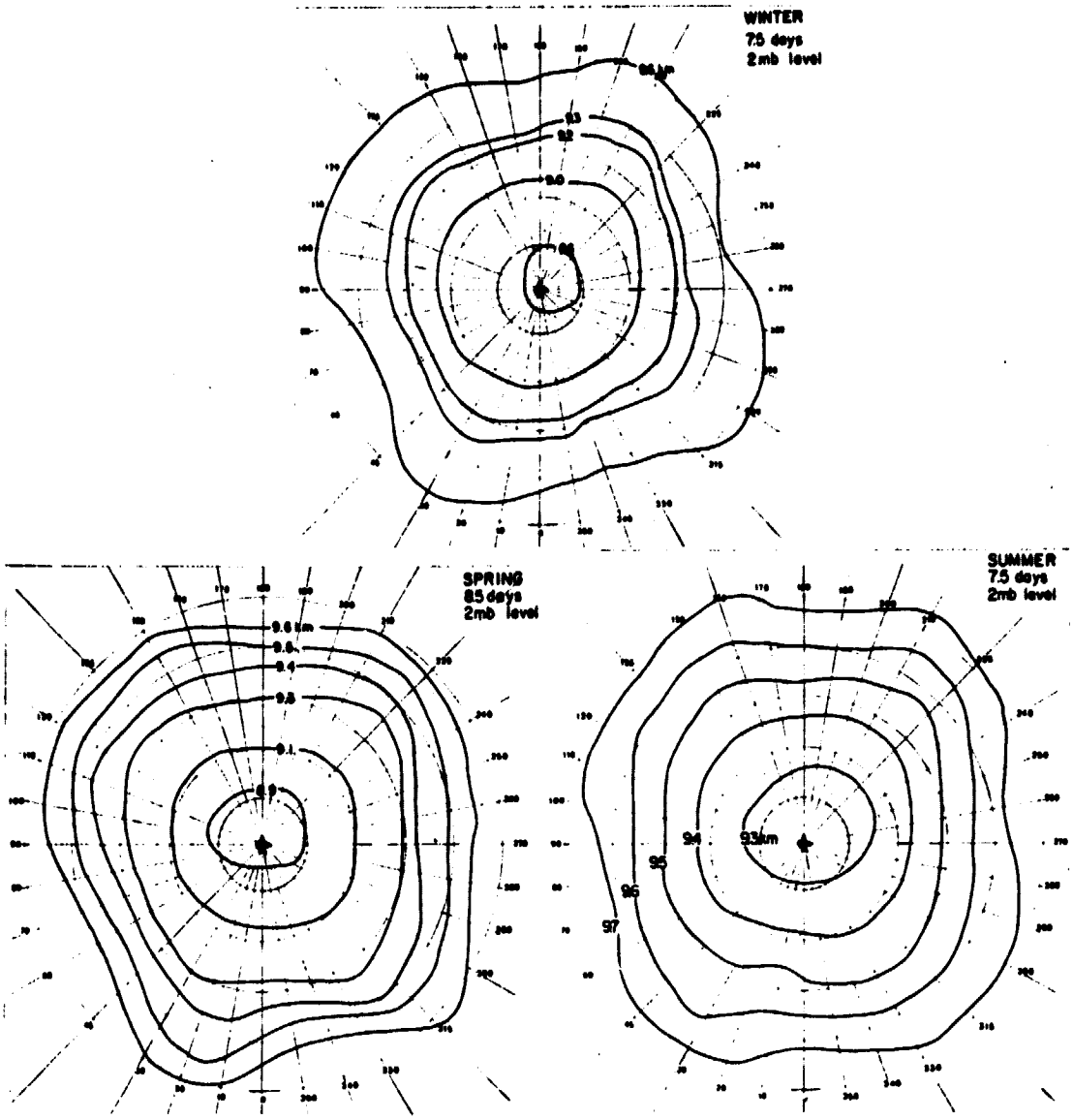
WINTER
7.5 days
2mb level
SPRING
85 days
2mb level
SUMMER
7.5 days
2mb level

Figure 6

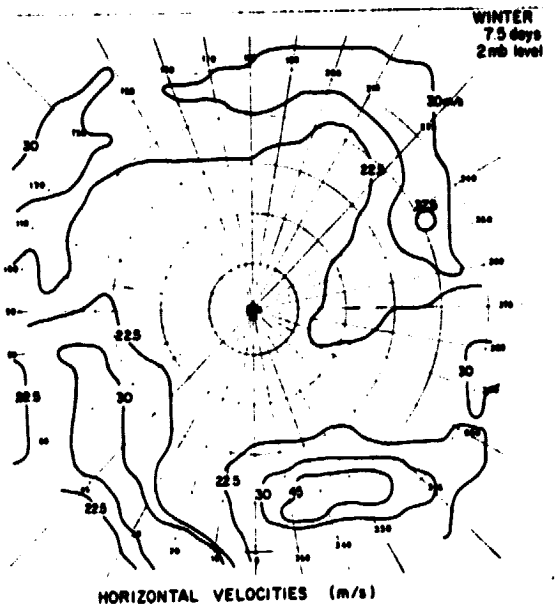

Figure 7

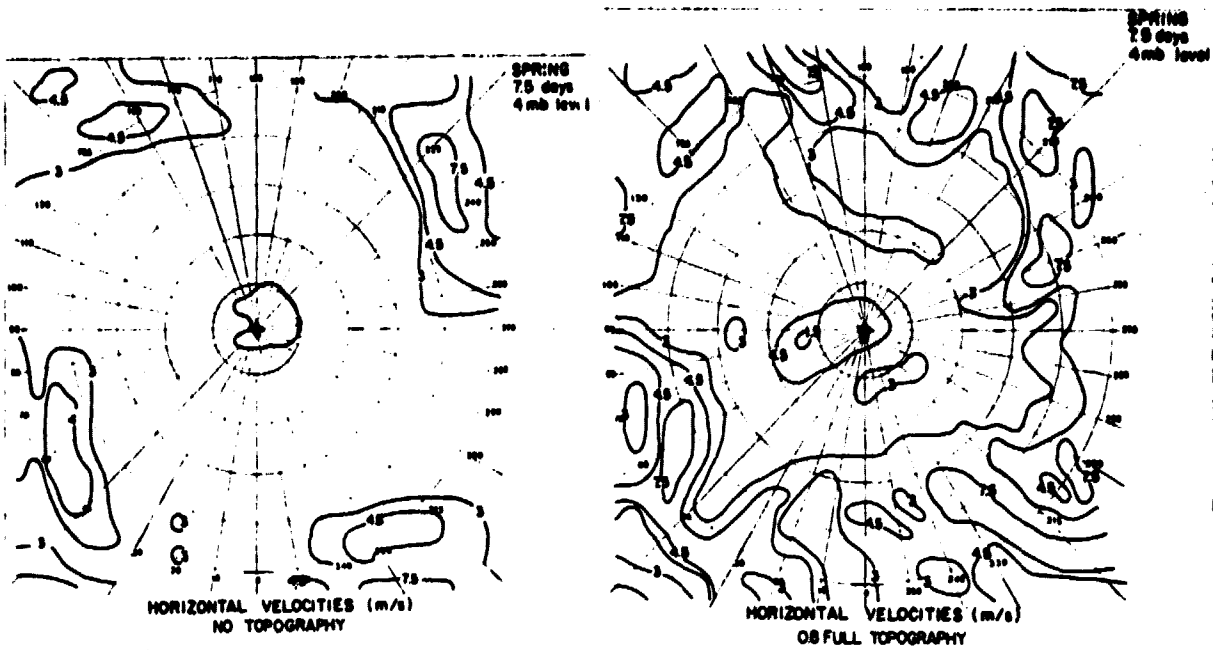
SPRING
7.5 days
4 mb level
HORIZONTAL VELOCITIES (m/s)
NO TOPOGRAPHY
SPRING
7.5 days
4 mb level
HORIZONTAL VELOCITIES (m/s)
OB FULL TOPOGRAPHY

Figure 8

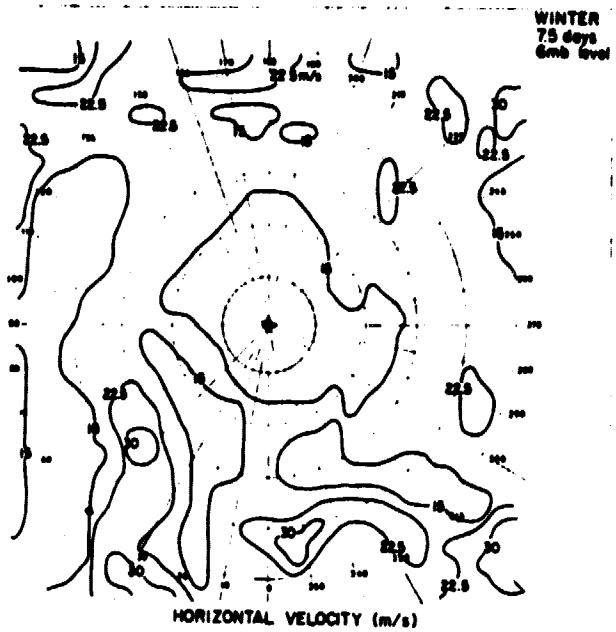

Figure 9

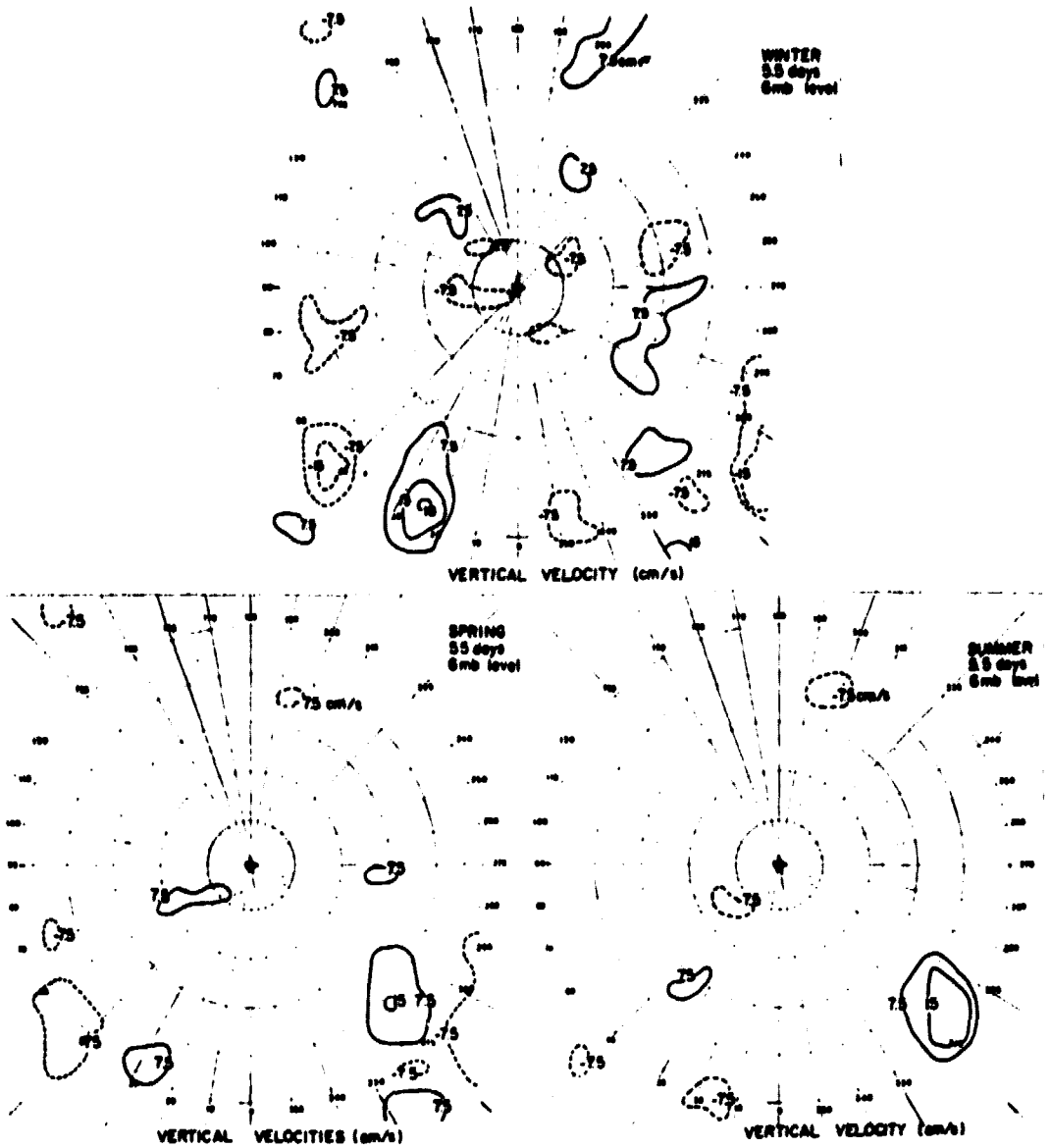
WINTER
5.5 days
6mb level
VERTICAL VELOCITY (cm/s)
SPRING
5.5 days
6mb level
VERTICAL VELOCITIES (cm/s)
SUMMER
5.5 days
6mb level
VERTICAL VELOCITY (cm/s)

Figure 10

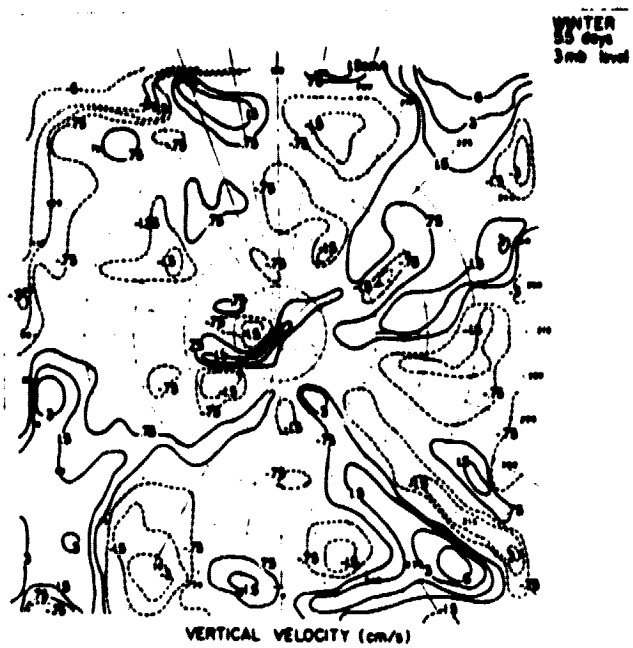
WINTER
5.5 days
3mb level
VERTICAL VELOCITY (cm/s)

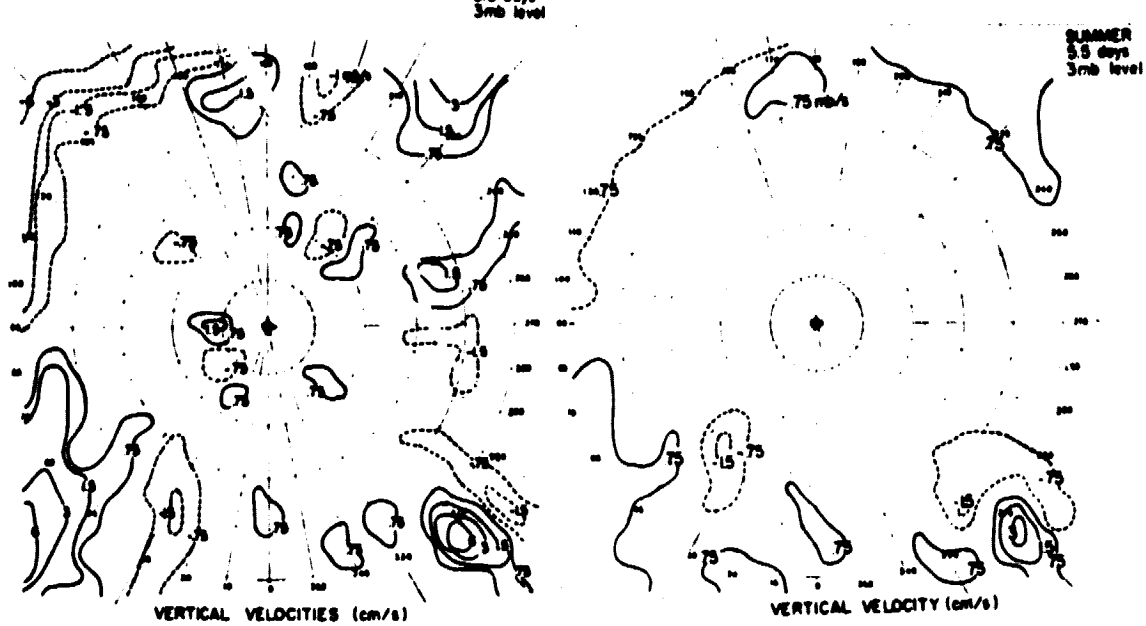
SPRING
5.5 days
3mb level
VERTICAL VELOCITIES (cm/s)
SUMMER
5.5 days
3mb level
75 mb/s
VERTICAL VELOCITY (cm/s)

Figure 11